Design and Kinematics Analysis for the SMU Haptic Glove

Ammar Yacoub[a], Edmond Richer[b] and Yildirim Hurmuzlu [a,*]

[a]Systems Laboratory, Southern Methodist University, Dallas, 75205, TX, USA
[b]Biomedical Instrumentation and Robotics Laboratory, Southern Methodist University, Dallas, 75205, TX, USA

ARTICLE INFO

Keywords:
Haptic Glove, Robotic Exoskeleton, Force feedback device, Motion Capture, Virtual Palpation, Haptic Palpation.

ABSTRACT

This paper presents the mechanical design and kinematic analysis of SMU Haptic Glove, which incorporates seven degrees of freedom (DOF) that are pneumatically actuated and developed for 3D elastographic imaging virtual palpation. The work is focused explicitly on kinematics and system architecture; full dynamic analysis, which was partially addressed in our previous study, is beyond the scope of this paper. This paper outlines the mechanical design of the SMU Haptic Glove The two-dimensional workspace for each finger and the glove's three-dimensional workspace are determined from the actuator positions using closed-form expressions based on the design geometry and are measured using embedded linear sensors. The accuracy of fingertip location, obtained from the linear sensors embedded in each finger joint design, is analyzed through two experiments. The first experiment compares fingertip positions from the sensors with those recorded by a five-camera OptiTrack motion capture system, examining each finger individually. The second experiment evaluates the overall accuracy of the glove in three dimensions via a size identification test.

1. Introduction

Medical palpation is a technique used by physicians during physical examinations, where they use their fingers to touch and assess various body parts to evaluate their size, shape, consistency, and location, relying on tactile feedback [41, 4]. The examination includes prehensile actions like grasping and seizing, as well as nonprehensile movements such as pushing and lifting. Its purpose is to identify and verify anatomical landmarks, including bones, muscles, and pulses, and detect abnormalities in soft tissues [41]. Palpation is commonly used for the initial detection and screening of bodily abnormalities, helping to diagnose life-threatening conditions such as cancer, abdominal aortic aneurysm, and acute appendicitis [20].

Despite its utility, palpation has notable limitations. It is primarily effective for superficial pathologies [17], as the ability to detect lesions decreases with increasing depth due to interference from overlying tissue layers. Furthermore, the inherent elasticity of certain structures can make them difficult to discern via palpation, especially for examiners with average tactile sensitivity [31]. Beyond these physical constraints, palpation inherently provides qualitative rather than quantitative assessments. Finally, its diagnostic accuracy relies heavily on the practitioner's sensitivity and experience, requiring significant expertise and training [35].

Moving beyond subjective assessments and physical constraints, elastography, also referred to as elasticity imaging, emerged in the 1990s and is designed to map tissue stiffness and the elastic properties of tissues by assessing how much they deform when exposed to an external force [17]. This technique effectively addresses many limitations of palpation by enabling the examination of deeper organs [17]. Furthermore, it quantitatively visualizes Young's modulus, which represents stiffness, offering robust data on tissue stiffness. Consequently, it guarantees standardized outcomes, reducing variability among examiners [17]. The most notable techniques include ultrasound and magnetic resonance imaging (MRI), both of which are essential for diagnosing cancerous tumors and conditions such as liver disease [24], breast cancer [29], thyroid nodule [37], and prostate cancer [8].

Enhancing how clinicians interpret and interact with these elastographic findings, recent advancements in computer technology, imaging methods, and nonlinear control algorithms allow for interaction with elastographic images via a haptic interface. This innovation provides a unique opportunity for medical professionals to virtually palpate suspected malignant tumors or other abnormal tissues within the human body using haptic devices [31].

Haptic systems deliver virtual sensations to users, allowing interaction with virtual environments or teleoperated systems [26]. They have been successfully utilized in applications such as virtual reality surgical training [16], robot-assisted surgery [12], and rehabilitation [10]. However, the current methods for palpating elastographic images [31], and most palpatory training using a virtual palpation simulator [41, 44], employ haptic interfaces that typically involve basic styluses or simple tactile displays like the Phantom, which enable single-point palpation. The limitation of this type of interface restricts the haptic palpation of elastographic images. To empower doctors to fully employ their training and experience in medical palpations, it is essential to have a haptic interface that incorporates multi-point palpation, representing the fingertip locations of the doctors, such as a haptic glove.

Many haptic gloves have been proposed [9, 19, 39, 28]. However, most utilize a straightforward finger-bending model that is adequate for approximating the grasp of a virtual object and providing realistic force feedback to the operator. Furthermore, many of these gloves do not control

*Corresponding author.
hurmuzlu@lyle.smu.edu (Y.H.)
ORCID(s):

Preprint not peer reviewed

This preprint research paper has not been peer reviewed. Electronic copy available at: https://ssrn.com/abstract=6350469

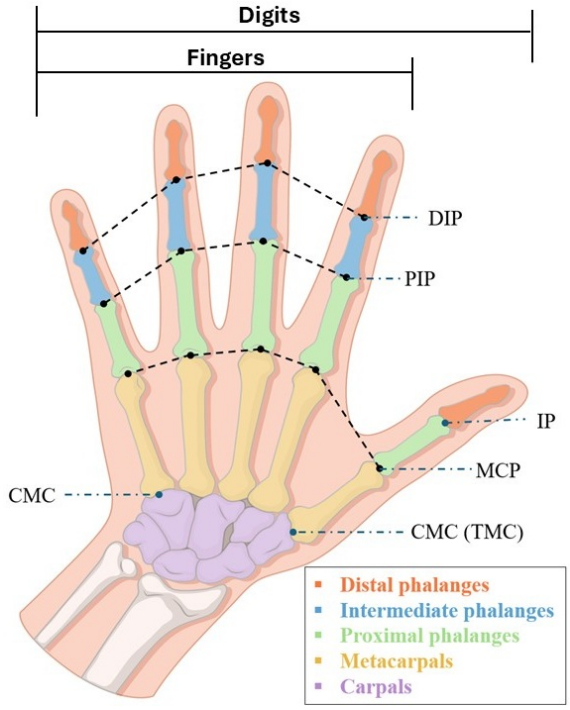

Figure 1: Bones and joints of the left human hand. (Adapted from https://www.freepik.com/free-vector/bone-inside-human-hand_22725580.htm)

all degrees of freedom in the fingers; instead, they depend on the collective movement of the finger joints. This approach leads to multiple fingertip positions corresponding to the exact location of the haptic actuators, significantly limiting their capacity to render force direction at the fingertip.

We aim to develop a system for virtual palpation of 3D elastographic medical images using a haptic glove that uniquely determines the fingertip's location, can palpate through multiple interaction points. In the first stage, we have created a haptic glove called SMU Haptic Glove, which is able to render directional force at the fingertips, responds to subtle joint movements with minimal sensors and actuators, while ensuring user comfort and freedom of movement. In this work, we concentrate on the system's mechanical design and kinematic modeling. A complete dynamic analysis, previously introduced in an earlier study for one finger, [38], is intentionally excluded here to maintain focus on establishing the system's design foundations and kinematic accuracy.

This paper is organized as follows: Section II provides a brief overview of hand anatomy. Section III details the existing haptic gloves. The design and kinematic analysis of the SMU Haptic Glove are discussed in Section IV, while Section V highlights the experimental aspects. Finally, Section VI presents the conclusion and future work.

2. Anatomy of the hand

The human hand consists of five digits, 27 bones, and 27 joints [23], as illustrated in Fig. 1. The bones include eight carpal bones that form the wrist, five metacarpals that

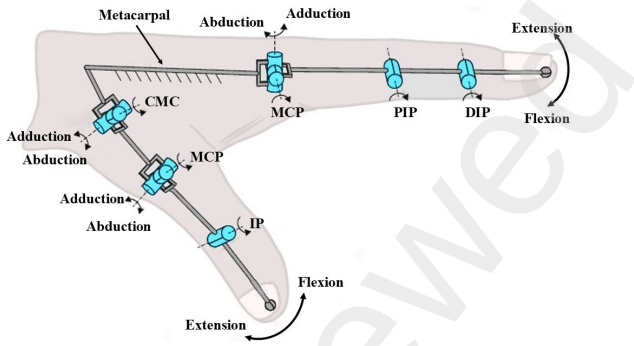

Figure 2: URR and UUR kinematic chain models of the index finger and thumb, respectively. (Adapted from [40])

shape the palm, and 14 phalangeal bones for the digits (three for each finger and two for the thumb). The hand's joint structure includes 14 joints for the digits (each finger has a metacarpophalangeal (MCP), proximal interphalangeal (PIP), and distal interphalangeal (DIP) joint, while the thumb contains an MCP and an interphalangeal (IP) joint), five carpometacarpal (CMC) joints, and additional joints associated with the carpal bones.

The human finger can be modeled as a kinematic chain consisting of three links, a universal joint followed by two revolute joints (URR kinematic chain), as illustrated in Fig. 2. The MCP joint serves as a two degree-of-freedom (DOFs) universal joint (U), enabling both flexion/extension and abduction/adduction movements, whereas the PIP and DIP joints are one DOF hinge (R) joints that allow for flexion and extension. The thumb can be modeled as a UUR kinematic chain since the CMC acts as a two DOFs universal joint (U).

3. Background and Related Works

Over the past decade, numerous mechanisms for haptic gloves (see [42] and Fig. 3 for examples) that provide force feedback have been developed and widely adopted in various fields, including virtual reality surgical training [16], robot-assisted surgery [12], and teleoperation [25]. Haptic gloves can be categorized based on their operational principles into active force feedback systems [21, 15] that employ actuators of various types, and passive force feedback systems, which create resistive forces using mechanisms such as brakes [7, 5], clutches [25], or string jamming [30].

A haptic glove system consists of two core components: an actuation unit that generates power and a transmission mechanism that delivers this power to the user's fingers. The actuation unit typically employs electric motors [3] or pneumatic systems [6], while the transmission techniques mainly fall into three categories: rigid transmissions utilizing linkages or gears [39, 6]; flexible transmissions using cables or tendons [28, 1]; and soft transmissions utilizing compliant materials [43]. The choice among these methods

This preprint research paper has not been peer reviewed. Electronic copy available at: https://ssrn.com/abstract=6350469

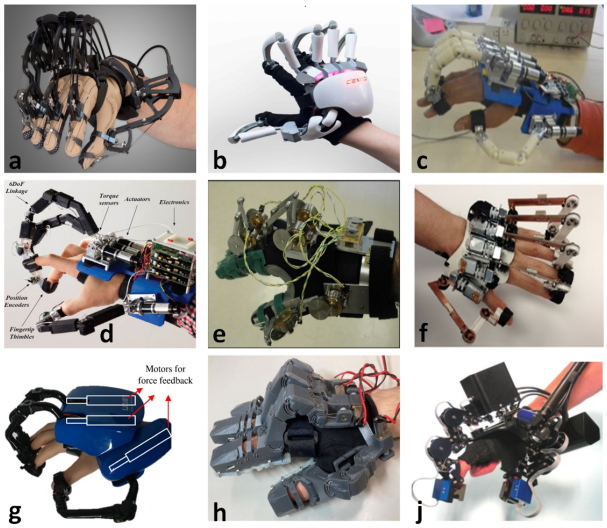

Figure 3: Previously developed haptic systems: (a) [9]; (b) [11]; (c) [22]; (d) [39]; (e) [5]; (g) [33]; (f) [3]; (h) [30]; (j) [14]

determines key performance characteristics of the glove, such as force fidelity and weight.

Another key design differentiator in haptic gloves is the scope of actuation. While some systems provide feedback to all five fingers [28], many designs focus on a subset, such as four fingers [22] or a three-finger configuration [39, 5]. To enable interaction, these gloves must also track the kinematic state of the user's hand. Commonly used sensors include magnetic Hall effect sensors, rotary encoders [6, 33, 39], potentiometers [32], and optical time-of-flight sensors [7].

Passive feedback force systems provide advantages in safety and low weight. However, they have difficulty simulating the variable stiffness of virtual objects, which is essential for realistic haptic interactions. Active force feedback systems address this limitation, as they can offer adaptable stiffness and a broader range of feedback forces [34].

The selection of the transmission mechanism directly affects performance, creating a trade-off between linkages and flexible designs. Linkage mechanisms provide a dependable solution by directly transferring forces and motions from actuators to finger joints, allowing for high-force output and precise control. On the other hand, flexible transmission systems, like cable-driven designs, face challenges such as friction-induced nonlinearity, cable wear that results in tension loss, and hysteresis, all of which undermine control accuracy and system reliability [27].

A foundational example is the CyberGrasp [9], introduced in the early 1990s, which provides unidirectional force feedback through a cable-driven mechanism. While well-known, its utility is restricted by this one-way force and the absence of integrated position sensors, necessitating a separate data glove (CyberGlove) for kinematic tracking. Another commercial glove is Dexmo by Dexta Robotics, which evolved from a passive, brake-based prototype [19] designed to simulate the resistance of virtual objects into a fully active glove [11]. The final version integrates servomotors for variable force feedback and can track 11 DoFs (3 for the thumb, 2 for each of the other fingers); however, its high cost can be a barrier to widespread adoption.

The landscape of non-commercial haptic gloves showcases a diverse range of design philosophies aimed at balancing performance, complexity, and ergonomics. The Rutgers Master II [6] features four pneumatic actuators arranged within the palm, along with Hall effect and infrared sensors for measuring position. While the design is compact and lightweight, its operational range is limited by the placement of the actuators. Iqbal et al. [22] introduced a four-finger glove featuring a directly driven, under-actuated (RR) mechanism that provides a single degree of freedom (DOF) of actuation, using rotary encoders for joint position tracking. Sarakoglou et al. [39] presented a three-finger, 6-DOF mechanism notable for its high degree of underactuation, where a single geared DC motor drives the entire kinematic chain to enable full tracking of the fingertip's position and orientation. Z. Ma and P. Ben-Tzvi [28] developed a five-finger glove where each finger is actuated by a six-bar linkage mechanism. A cable-driven transmission, powered by a dedicated geared DC motor, delivers force to each finger, and the system is capable of calculating fingertip position. Park et al. [33] introduced WeHAPTIC, a three-finger glove that uses a DC motor-driven linkage for force transmission and incorporates Hall sensors and motor encoders for kinematic tracking. This integrated sensing allows the device to calculate the position of the fingertip directly and to estimate joint angles for the thumb and index fingers via custom algorithms.

Table 1 compares the capabilities of our proposed design with several state-of-the-art force-feedback gloves. Many existing designs have one actuator per finger, conflating the flexion/extension motion of all finger joints into one underactuated mechanism. While this straightforward approach is sufficient for simulating object grasping in virtual environments, where interaction relies mainly on fingertip positions, it inherently limits the ability to control the finger posture. Consequently, multiple fingertip locations may map to the same haptic actuator position, significantly constraining the system's ability to render precise force direction at the fingertips.

For finger-joint tracking, some systems employ a separate glove to measure joint angles [47, 9], while others require users to measure finger lengths and perform calibration prior to use [28, 34]. Alternative approaches include interpolation-based methods [19] and lookup-table solutions [6]. Additionally, some existing works report only the intrinsic resolution of the sensor, while our values incorporate the overall system performance, including sensor noise, mechanical backlash, and DAQ system resolution.

To address these limitations, we introduce the SMU Haptic Glove, a novel device engineered for high-fidelity haptic interaction. Our primary contribution is a design offering 2-DOF actuation per finger, enabling more sophisticated control over finger posture. In addition, the system

This preprint research paper has not been peer reviewed. Electronic copy available at: https://ssrn.com/abstract=6350469

Table 1
Kinematic comparison of typical existing kinesthetic gloves and the proposed glove.

Reference	Actuated Fingers	Motion Range	Actuator Type	Transmission Method	Actuated DoF	Sensor Type	Resolution	Sampling Rate	Fingertip Tracking	Joint Angle Tracking	Weight	Attachment Method	Hand size adjustable
SMU Haptic Glove	3	Full flexion from 0° extension	Pneumatic	Linkage	6	Linear sensor	< 0.3°	1 kHz	Yes	Yes	870g	Finger cap	Yes
HIRO III [13]	5	Thumb:705cm^3, Other:587cm^3	DC Motor	Gear-based mechanisms	15	Encoder	N.A.	1kHz	Yes	Yes	900g	Finger holder	Yes
CyberGrasp [9]	5	Full hand closing	DC Motor	Tendons	5	Separate CyberGlove	< 1°	112 records/sec	Yes	Yes	450g	Finger cap	Yes
RMII-ND [6]	4	28-44 mm piston stroke	Pneumatic	Linkage	4	IR and Hall effect	0.45°	435 records/sec	Yes	Yes[4]	80g	Finger cap	Yes
Wolverine [7]	4	Virtual shpere with 20-160 mm diameter	DC Motor	Brake mechanism	3	Time-of-Flight (ToF) sensors and IMU	N.A.	100Hz	Yes	No	55g	Velcro belt	Yes
Dexmo [19]	5	N.A.	Micro servo	locking mechanism	5	Rotational sensors	0.5°	20Hz	Yes	Yes[3]	270g	Finger cap	No
DESR [46]	4	5 mm piston stroke	Dielectric elastomer	–	3	Laser sensor	N.A.	N.A.	N.A.	N.A.	38g	Finger cap	Yes
RML Glove [48]	2	Full flexion/extension	DC Motor	Cable	2	Hall sensor	0.4°	1.3 kHz	Yes	Yes[1]	180g	Finger cap	Yes
Jamming tubes[49]	2	Full flexion/extension	Pneumatic	Jamming	N.A.	Sensor glove	N.A.	N.A.	Yes	Yes	40g	Glove	NO
SAFE [28]	5	Maximum of 150deg	DC Motor	Cable	5	Encoder	N.A	300Hz	Yes	Yes[1]	310g	Elastic band	Yes
HEXOSYS[21]	2	N.A	DC Motor	Linkage	2	Encoder	0.08°	N.A.	N.A.	N.A.	400g	Velcro belt	No
WeHAPTIC [33]	3	Full flexion/extension	DC moto	Linkage	3	Hall sensor	N.A.	1 kHz	Yes	Yes[2]	488g	Finger holder	Yes
EFFG [34]	5	Substantial portion (linear actuator motion range is 16 mm)	Servo Motor	Push–pull cable mechanism	5	Sensory enabled motor	N.A.	0.96 kHz	Yes	Yes[1]	278g	Velcro belt	N.A.
HEXOTRAC [39]	3	Full flexion/extension	DC Motor	Linkage	3	Magnetic encoder	< 0.087°	1kHz	Yes	NO	N/A	Finger cap	Yes
[2]	3	Full flexion/extension	DC Motor	Bowden Cable	3	Magnetic encoder	N.A.	N.A.	Yes	NO	400g	Velcro belt	Yes
HEXOSYS II [22]	4	Full flexion/extension	DC Motor	Linkage	4	Magnetic encoder	0.08°	N.A.	Yes	NO	460g	Velcro clip	Yes
[14]	2	N.A.	DC Motor	Steel Cable	6	N.A.	N.A	N.A.	N.A	Yes	1.1kg	Finger cap	N.A
[47]	5	Full hand closing	Pneumatic	Cam-linkage	5	Separate data glove	0.02°	70Hz	Yes	Yes	245g	Finger holder	NO

[1] Finger phalanx lengths must be known. [2] Calibration is needed to measure finger lengths for user-specific customization. [3] Interpolation assumes DIP and PIP joint angles depend on the MCP angle x via functions f(x) and g(x). [4] Using lookup table.

calculates joint motion using closed-form bijective transfer functions that map actuator displacements to joint angles and fingertip locations. This approach eliminates the need for user-specific calibration, external tracking devices, or iterative numerical solvers, enabling real-time computation of fingertip pose. As a result, the SMU Haptic Glove supports more realistic haptic rendering by enabling directional fingertip force control than what is achievable with conventional 1-actuator-per-finger systems.

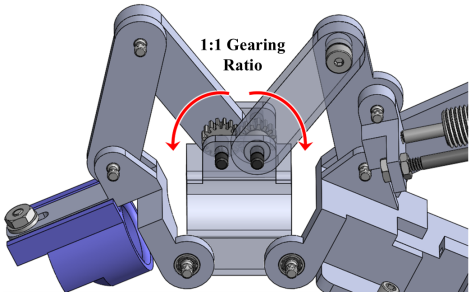

Figure 4: Gearing linkage system for index and middle fingers.

4. Glove Design and Kinematic Analysis

The SMU Haptic Glove illustrated in Fig. 5 was developed at the Lyle School of Engineering [15]. The architecture was specifically designed to provide both powerful and precise force feedback, a combination essential for virtual palpation tasks. To achieve this, our design synergistically integrates pneumatic actuators with rigid linkage transmissions. Pneumatic actuators were chosen for their superior power-to-weight ratio, enabling ample force capacity. The rigid linkages ensure that this power is transmitted to the user with high fidelity, precision, and minimal loss.

The design of the SMU Haptic Glove consists of four main substructures: the index finger substructure, the middle finger substructure, the thumb substructure and the palm substructure. The glove is mounted on the dorsal side of the hand and interfaces with the distal phalanges of the user's index, middle fingers, and thumb using a single-attachment method. These fingers, used primarily during palpation, possess 13 (DOFs). To simplify the design while meeting palpation requirements, six degrees are actuated and measured, one degree is measured without actuation, and two DOFs are coupled with others using a 1:1 gear mechanism as shown in Fig. 4, resulting in a total of 7 DOFs (as detailed in Table 2). The active joints are driven

This preprint research paper has not been peer reviewed. Electronic copy available at: https://ssrn.com/abstract=6350469

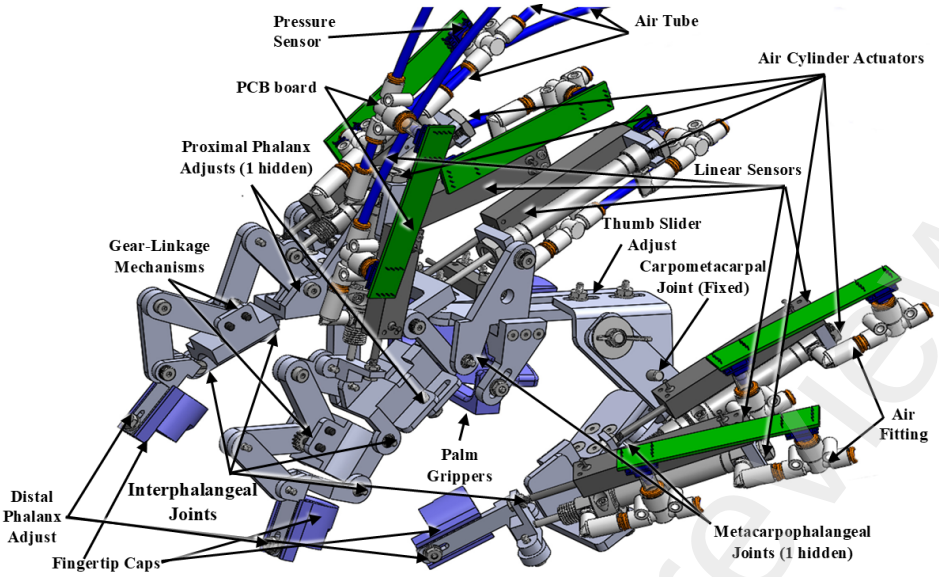

Figure 5: SMU Haptic Glove CAD representation; including mechanical, electronic, and pneumatic components [45].

Table 2
Joint actuation table for index and middle fingers, and thumb.

Joint Name	Movement Type	Index Finger	Middle Finger	Thumb
Distal Interphalangeal	Flexion/Extension	Constrained (via gearing mechanism)		—
Proximal Interphalangeal (θ_{j2})	Flexion/Extension	Actuated	Actuated	Actuated
Metacarpophalangeal (θ_{j1})	Flexion/Extension	Actuated	Actuated	Actuated
Metacarpophalangeal (θ_{j3})	Abduction/Adduction	Measured	Fixed	Fixed
Carpometacarpal	Flexion/Extension	—	—	Fixed
Carpometacarpal	Abduction/Adduction	—	—	Fixed

Table 3
Adjustable lengths of the phalangeal segments for the index and middle fingers, and the thumb.

Digit	Phalangeal Segment	Range [mm]
Index	Proximal (d_{11})	36.5–49.0
	Distal (d_{12})	20–25
Middle	Proximal (d_{21})	38.5–50.5
	Distal (d_{22})	22–28
Thumb	Proximal (d_{31})	28.0–34.0
	Distal (d_{32})	23–30

by pneumatic cylinders, with linear sensors aligned with the cylinders to measure their stroke.

The design emphasizes accommodating various hand sizes. Even within a single individual, hands can differ in size and shape and are not perfectly symmetrical [36]. The glove features nine adjustable connections, strategically placed to align with key areas of the hand, provided by statistical measurements from the Hand Anthropometry of U.S. Army Personnel [18]. These adjustments allow the glove to fit a wide range of users, encompassing the upper 75% of the female population and the lower 75% of the male population based on statistical data.

The nine adjustable connections are organized into two categories. The first category corresponds to the lengths of the proximal and distal phalanges of the finger. The available ranges for these segment lengths are provided in Table 3. The second second consists of adjustable connections that modify finger positioning. Specifically, the middle finger substructure can shift laterally by up to 14 mm on the central

Preprint not peer reviewed

This preprint research paper has not been peer reviewed. Electronic copy available at: https://ssrn.com/abstract=6350469

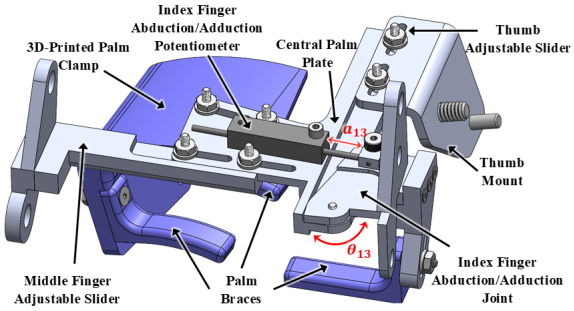

Figure 6: Palm substructure viewed from the fingertip perspective [45].

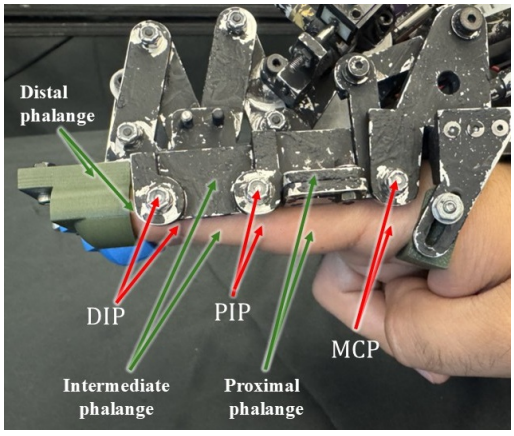

Figure 7: Scheme of the anthropomorphic kinematics of the index substructure.

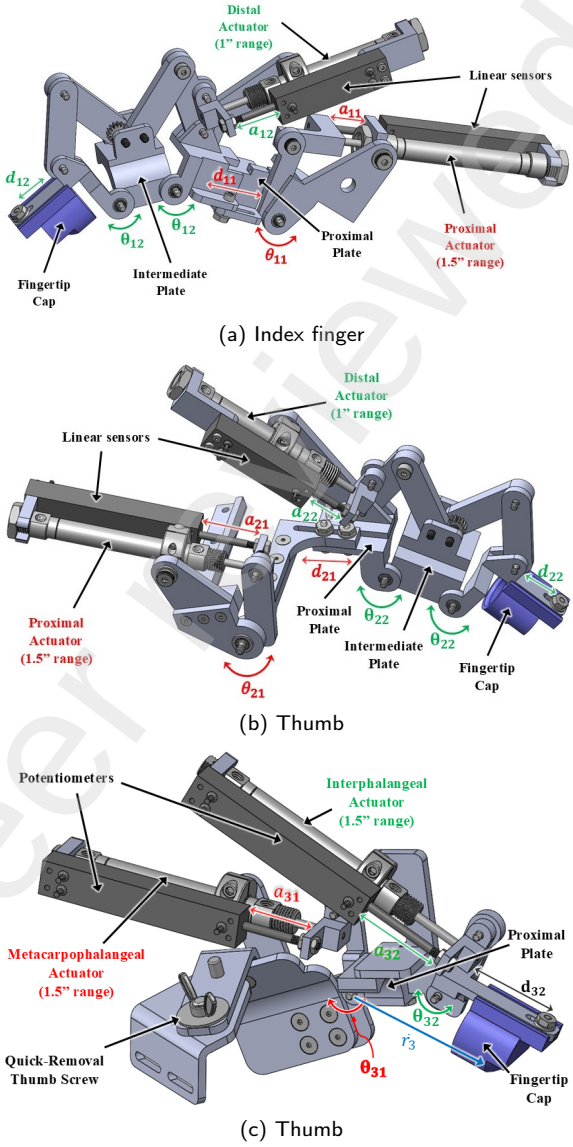

Figure 8: Substructure design and actuated degrees of freedom of: (a) Index finger, (b) middle finger, (c) Thumb.

palm plate, allowing adjustment of the distance between the MCP joints of the index and middle fingers. In addition, the thumb substructure incorporates an adjustable connection that enables vertical movement of up to 13.5 mm along the central palm plate. This adjustment accommodates users with varying hand sizes by modifying the distance between the index finger MCP joint and the thumb CMC joint. The final adjustment addresses palm size by altering the positions of the palm braces and the palm clamp (see Fig. 6)

4.1. Substructure Design

The kinematic design of the SMU Haptic Glove finger is defined as anthropomorphic kinematics [14], which simulates finger movement by attaching its components sequentially to the finger's phalanges, as shown in Fig. 7. The substructure of the index finger shown in Fig. 8a consists of several curved plates that partially wrap around each phalanx of the user's finger, along with a linkage system positioned above the phalanges to transmit force from two pneumatic actuators. The proximal phalanx plate connects to the pivot plate via a shoulder screw passing through a ball bearing, forming an axle that enables bending motion. This plate comprises two components mounted on an adjustable track and secured with a bolt. Moving distally along the substructure, a fixed-length intermediate phalanx plate connects to a distal phalanx mounting arm, to which a finger cup is attached via another adjustable track to support the fingertip. A set of linkages is mounted above the intermediate and distal phalanx plates; however, unlike the MCP joint, the two IP joints cannot move independently. Instead, they are mechanically linked by a pair of 16-tooth nylon gears in a 1:1 ratio, actuated by the distal pneumatic cylinder located on the proximal phalanx plate and connected to the IP linkage system.

The design of the middle finger substructure, illustrated in Fig. 8b, closely resembles that of the index finger substructure. The primary differences include its longer length, a mirrored design, and the fixed abduction/adduction motion of the MCP joint. Unlike the index and middle fingers, the thumb (see Fig. 8c) does not feature a gear mechanism because it has only one IP joint. Additionally, both the abduction/adduction of the MCP joint and the flexion/extension

This preprint research paper has not been peer reviewed. Electronic copy available at: https://ssrn.com/abstract=6350469

and abduction/adduction of the CMP joint are fixed. A quick-release mechanism is also integrated, enabling users to easily detach the thumb substructure.

The three substructures are anchored to the central palm substructure with a unique connection, as shown in Fig. 6. The pivot joint of the index finger substructure allows the entire substructure to rotate, enabling the user to abduct the index finger up to 20° away from the middle finger. The middle finger and thumb substructures connect to the palm plate via two tracks. The central plate of the palm substructure is linked to the palm clamp that wraps around the human palm and is secured by three adjustable braces.

4.2. Kinematic Equations

The transformation functions that relate actuator positions, measured by linear sensors, to their corresponding joint angles were derived using a geometric analytical method (see Appendix A for the full derivation). In the following equations, the notation employs two subscripts: j indexes the finger (1=index, 2=middle, 3=thumb), while k indexes the joint motion (1 = MCP flexion/extension, 2 = proximal IP flexion/extension, 3 = MCP abduction/adduction

The flexion of the MCP joint (θ_{j1}) is calculated from its dedicated actuator's displacement (a_{j1}) as defined by Eq. 1. Similarly, the flexion of the IP joint (θ_{j2}) is determined from the displacement of the actuator (a_{j2}) via Eq. 2. For the index finger, the unactuated MCP abduction/adduction is given by Eq. 4.

$$\begin{aligned}\theta_{11} &= \cos^{-1}\left(1.092 - 2.895\times10^{-4}a_{11}^2\right) - 0.207\,\pi,\\ \theta_{21} &= \cos^{-1}\left(1.023 - 3.352\times10^{-4}a_{12}^2\right) - 0.232\,\pi,\\ \theta_{31} &= \cos^{-1}\left(1.107 - 2.996\times10^{-4}a_{31}^2\right) - 0.18\,\pi.\end{aligned} \tag{1}$$

$$\begin{aligned}\theta_{12} &= 2\cos^{-1}\left(\frac{25.38 - 33\cos\theta_{1g}}{\sqrt{1733.06 - 1674.97\cos\theta_{1g}}}\right) - 0.210\,\pi,\\ \theta_{22} &= 2\cos^{-1}\left(\frac{27.415 - 33\cos\theta_{2g}}{\sqrt{1840.56 - 1809.37\cos\theta_{1g}}}\right) - 0.269\,\pi,\\ \theta_{32} &= \cos^{-1}\left(1.058 - 3.036\times10^{-4}a_{32}^2\right) - 0.172\,\pi,\end{aligned} \tag{2}$$

where θ_{1g} and θ_{2g} are the angles of the gear mechanism constraining the proximal and distal IP joints.

$$\begin{aligned}\theta_{1g} &= \sin^{-1}\left(1.479 - 6.477\times10^{-4}a_{12}^2\right) + 0.509\,\pi,\\ \theta_{2g} &= \sin^{-1}\left(1.587 - 5.933\times10^{-4}a_{22}^2\right) + \frac{\pi}{2}.\end{aligned} \tag{3}$$

$$\theta_{13} = 0.349066 - \tan^{-1}\left(\frac{8.5 - 2.4a_{13}}{23.35}\right) \tag{4}$$

These closed-form equations represent bijective transfer functions, establishing a direct relationship between actuator displacement and joint angle. This relationship and the system's kinematic limits are visualized in Fig. 9.

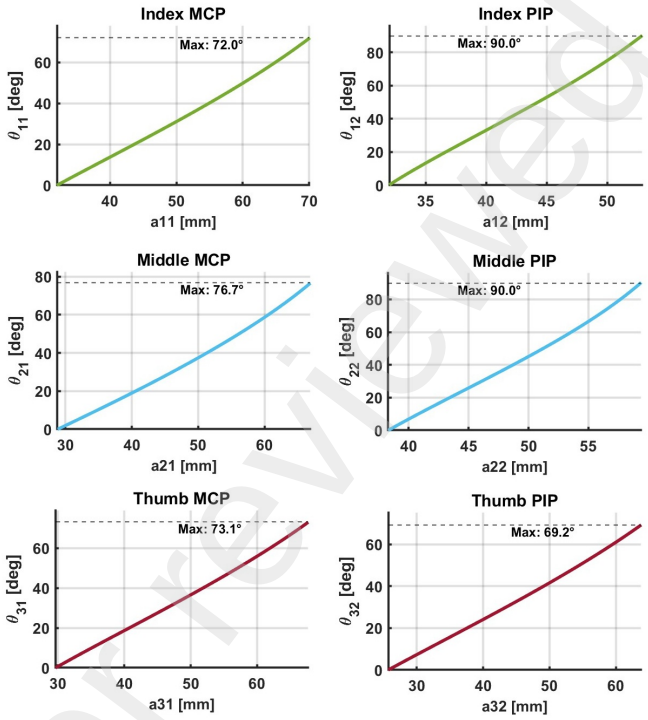

Figure 9: Joints angle of each finger based on their respective actuators.

The fingertip location vector $\bar{r}_j = [x_j, y_j]^T$ defined by Eq. 5 is computed from the MCP joint angle θ_{j1}, the IP joint angle θ_{j2}, the adjusted length of the proximal phalanx d_{j1}, and the adjusted fingertip length d_{j2}. Figure 10 illustrates the workspace of each digit. The coordinate frame for this analysis is defined with its origin at the MCP joint, its x-axis pointing distally along the outstretched finger, and its y-axis oriented in the direction of finger flexion.

$$\begin{aligned}\bar{r}_1 &= d_{11}\begin{bmatrix}\cos(\theta_{11})\\ \sin(\theta_{11})\end{bmatrix} + 25\begin{bmatrix}\cos(\theta_{11}+\theta_{12})\\ \sin(\theta_{11}+\theta_{12})\end{bmatrix} + d_{12}\begin{bmatrix}\cos(\theta_{11}+2\theta_{12})\\ \sin(\theta_{11}+2\theta_{12})\end{bmatrix},\\ \bar{r}_2 &= d_{21}\begin{bmatrix}\cos(\theta_{21})\\ \sin(\theta_{21})\end{bmatrix} + 31\begin{bmatrix}\cos(\theta_{21}+\theta_{22})\\ \sin(\theta_{21}+\theta_{22})\end{bmatrix} + d_{22}\begin{bmatrix}\cos(\theta_{21}+2\theta_{22})\\ \sin(\theta_{21}+2\theta_{22})\end{bmatrix},\\ \bar{r}_3 &= d_{31}\begin{bmatrix}\cos(\theta_{31})\\ \sin(\theta_{31})\end{bmatrix} + d_{32}\begin{bmatrix}\cos(\theta_{31}+\theta_{32})\\ \sin(\theta_{31}+\theta_{32})\end{bmatrix}.\end{aligned} \tag{5}$$

Figure 11 illustrates the three-dimensional workspace of the SMU Haptic Glove, defined as the spatial union of the two-dimensional workspaces of the individual fingers with respect to their mounting on the palm substructure.

5. Experimental verification

Accurate fingertip positioning is a prerequisite for rendering convincing haptic feedback in virtual palpation.

This preprint research paper has not been peer reviewed. Electronic copy available at: https://ssrn.com/abstract=6350469

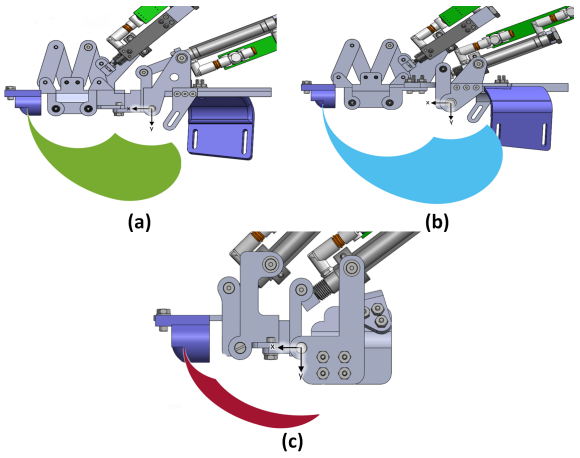

Figure 10: 2D planar workspace of: (a) Index finger, (b) Middle finger, and (c) Thumb [45].

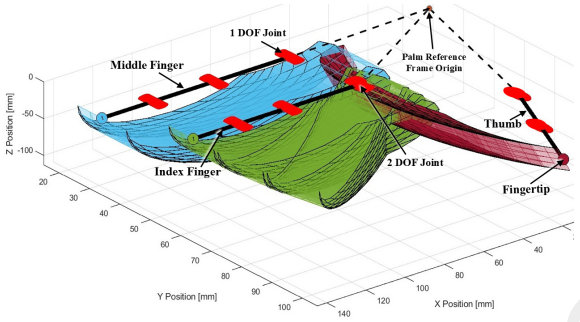

Figure 11: Three-dimensional workspace of the SMU Haptic Glove [45].

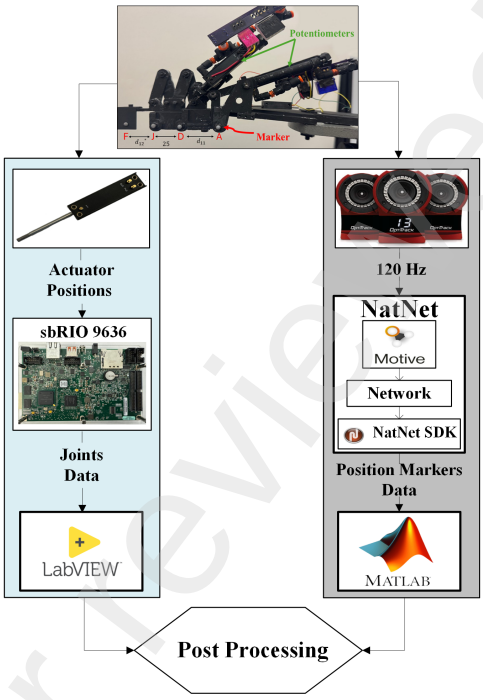

Figure 12: Overview of the experimental framework. The system computes fingertip location using an LMC13 linear potentiometer and an NI sbRIO-9636 controller. The MoCap system serves as ground truth, streaming marker position data from Flex 13 cameras to MATLAB for analysis [45].

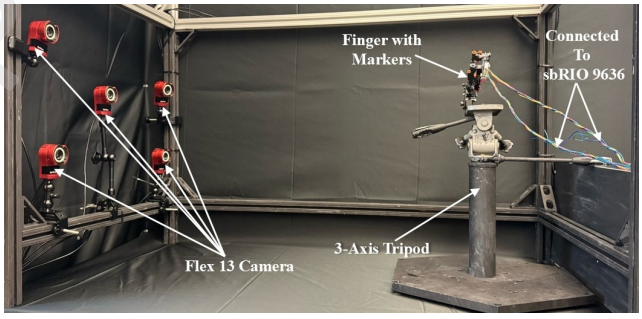

Figure 13: Experimental setup for system validation. The finger substructure, mounted on a 3-axis tripod for precise positioning, is monitored by a five-camera OptiTrack system [45].

Therefore, two experiments were designed to investigate the localization accuracy of the fingertip position obtained using Eq. 5 based on joint angles calculated from Eqns. 1, 2 with the actuators' stroke measured by linear position sensors.

5.1. Fingertip location using motion caption

A detailed description of the experimental setup and results is provided in [45]; the following subsections present a concise overview for readers' convenience.

5.1.1. Experimental Setup

The experimental framework, illustrated in Fig. 12, was designed to validate the precision of an embedded sensor system by comparing its measurements against a ground truth OptiTrack motion capture (MoCap) system. The embedded system calculates fingertip position from actuator displacement, which is measured by a P3 America LMC13 linear potentiometer. An NI sbRIO-9636 real-time controller processes these measurements, using a LabVIEW implementation of the forward kinematic model (Eq. 5) to compute the final location. Concurrently, the ground truth system, shown in Fig. 13, used five OptiTrack Flex 13 cameras to track 4 mm passive markers placed on the user's joints and a custom finger cap. The 3D coordinate data from these markers was streamed from the Motive Tracker 2.0 software to MATLAB, where the final reference fingertip position was calculated.

5.1.2. Results

Experiments were conducted for the index finger (210 samples) and thumb (142 samples). To ensure data quality, each measurement was averaged from 10 consecutive readings at 1 kHz, and this process was repeated 10 times per sample to assess repeatability. The results demonstrated high consistency. For the index finger, the maximum standard deviation (STD) across trials was 1.04 mm (x-position) and

This preprint research paper has not been peer reviewed. Electronic copy available at: https://ssrn.com/abstract=6350469

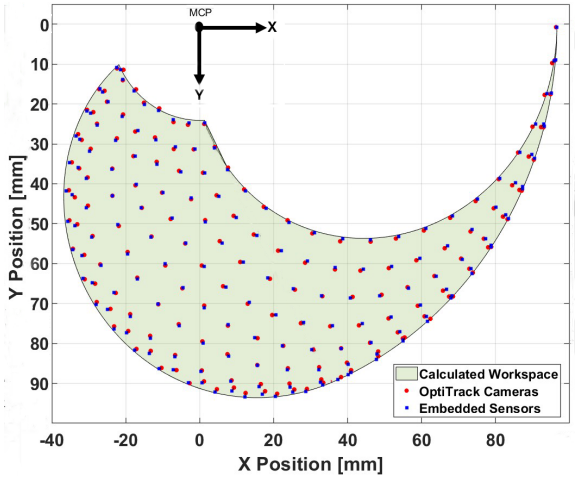

(a) Index finger

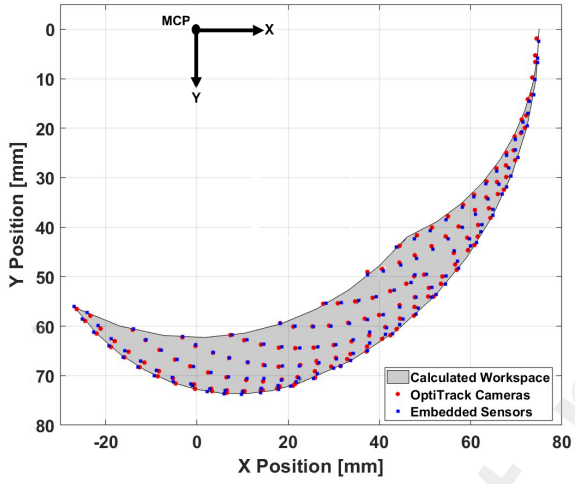

(b) Thumb

Figure 14: Comparison of position measurements using OptiTrack cameras and the embedded sensors for (a) index finger and (b) thumb.

0.70 mm (y-position), with a mean difference of approximately 0.3 mm for both axes. The thumb showed higher precision, with a maximum STD of 0.36 mm (x-position) and 0.41 mm (y-position), and mean differences of 0.27 mm and 0.17 mm for the respective axes. These low statistical values confirm a highly precise measurement process. The distribution of samples for index finger and thumb fingertip positions, measured with the OptiTrack cameras and calculated using the embedded sensors throughout the entire workspace, is shown in Fig 14.

A quantitative summary of the key error metrics is provided in Table 4. The results confirm a high degree of accuracy for both finger substructures, with all maximum absolute errors at or below 1.25 mm. The root mean square (RMS) errors consistently remained low, staying below 0.5 mm for all axes across both digits. This high precision is further highlighted by the fact that for the y-axis, over 73% of samples for both fingers had an error of less than 0.5 mm. Collectively, these findings validate the

Table 4
Fingertip position error metrics for index finger and thumb.

Digit	Axis	Max |Error|	RMS	STD	$N < 0.5$ mm
Index	X	1.25	0.41	0.30	126 (60%)
	Y	1.00	0.35	0.29	154 (73%)
Thumb	X	1.00	0.47	0.24	72 (51%)
	Y	1.00	0.30	0.17	106 (75%)

precision of the embedded sensor systems and the accuracy of the kinematic models for both the index and thumb.

To assess the overall positioning error, the analysis was extended from individual components to the vector magnitude, calculated as the Euclidean norm ($|\bar{r}| = \sqrt{x^2 + y^2}$). The RMS of the magnitude error was very low for both the index finger (0.38 mm) and the thumb (0.36 mm), while the standard deviation of the error was approximately 0.31 mm for both. Furthermore, the magnitude error was less than 0.5 mm for a large majority of samples: 77% (162 samples) for the index finger and 80% (115 samples) for the thumb. These results reinforce the findings from the component-wise analysis, confirming the system's high overall accuracy.

5.2. 3D Objects size estimation

The precision of 3D fingertip localization for the full glove, was assessed by an experiment conducted to identify the diameter of spherical and cylindrical objects of different sizes. During the experiment, a participant wearing the glove touched a spherical object with their index finger, middle finger, and thumb, as shown in Fig. 15. The 3D position of each fingertip was initially determined using Eq. 5. A custom MATLAB script transformed the fingertip vector into a palm-based coordinate frame, then calculated the sphere's center and radius by solving a constrained system of three nonlinear equations with four unknowns using the Optimization Toolbox. Custom hemispherical finger caps were utilized to simplify contact calculations.

Determining the sphere externally tangent to three given hemispheres is an instance of Apollonius's problem. As illustrated in Fig. 16, the solution is governed by two key constraints. First, a distance constraint (Eq. 6) dictates that the distance between the center of the unknown sphere and the center of each hemisphere must equal the sum of their respective radii. Second, a direction constraint (Eq. 7) ensures that the point of contact occurs on the convex side of each hemisphere:

$$\|\mathbf{C} - \mathbf{C}_{hi}\| = R + R_{hi}, \quad i = 1, 2, 3 \tag{6}$$

$$\mathbf{n}_i \cdot (\mathbf{C} - \mathbf{C}_{hi}) \leq 0 \tag{7}$$

where $\mathbf{C} = (C_x, C_y, C_z)$ and R denote the center and radius of the tangent sphere, both of which are unknown. $\mathbf{C}_{hi}$ and

This preprint research paper has not been peer reviewed. Electronic copy available at: https://ssrn.com/abstract=6350469

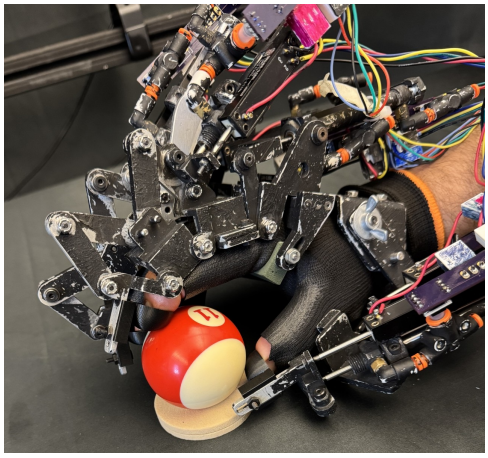

Figure 15: A participant wearing the SMU Haptic Glove touches a ball during the 3D object size estimation experiment.

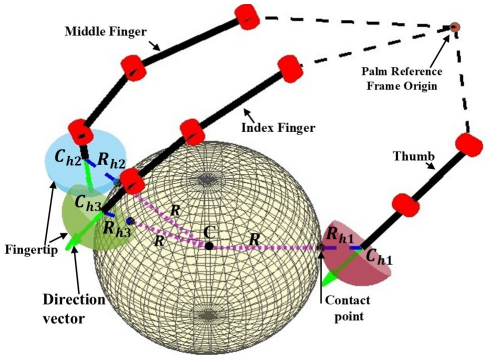

Figure 16: Visualization of the estimated sphere that externally tangents all three finger caps.

Table 5
Sphere size estimation error metrics

Actual radius [mm]	RMS error	Max |Error|	Min |Error|
25 (Wooden)	0.4815	0.9183	0.1564
28.575 (Billiard)	0.5306	0.8559	0.0528
22.225 (Bearing)	1.0258	1.3750	0.3441
34.925 (Bearing)	0.8337	1.1118	0.3967
25.4 (Bearing)	0.6367	0.8683	0.3252

R_{hi} represent the known center and radius of the tangent sphere. $\mathbf{n}_i$ indicates the outward normal of the flat face of the hemisphere.

The experiment was conducted using several balls with precisely known diameters, including ball bearings and a billiard ball. The experimental procedure required a user to touch each sphere five times at different locations. The resulting accuracy of the sphere size estimation is presented in Table 5, while Fig. 16 offers a visual reconstruction of an estimated sphere tangent to the three finger caps.

Table 6
Cylinder size estimation error metrics

Actual radius [mm]	RMS error	Max |Error|	Min |Error|
30.00	0.6474	0.9782	0.0496
25.40	0.3776	0.7661	0.0439
19.05	0.6517	1.1581	0.1925

The experiment has been extended to determine the diameter of a cylindrical object with a known height and defined radius boundary, with the results shown in Table 6.

For all tested objects, the RMS error for the estimated radius remained consistently low, only reaching a maximum of 1.03 mm in one trial. This performance underscores the effectiveness of the glove's design and the accuracy of the method employing the embedded sensors and geometrical analysis in pinpointing the fingertip location.

6. Conclusion

This paper presents the design, kinematic modeling, and experimental validation of the SMU Haptic Glove, a novel device providing 2-DOF actuation per finger. We established a comprehensive kinematic model with bijective transfer functions and closed-form equations for fingertip localization and workspace analysis. The system's accuracy was rigorously validated against a motion capture system, demonstrating high precision. For individual finger tracking, the RMS error of the fingertip position vector was as low as 0.36 mm. Additionally, the accuracy for the complete glove has been validated through an identifying object sizes experiment, where the maximum RMS error is approximately 1.03 mm. The demonstrated accuracy combined with the ability to uniquely determine the fingers' posture, affirms our design as a promising platform for a more realistic haptic rendering and interaction in virtual environments.

The study provides a detailed examination of the system's design and kinematic performance. A full dynamic analysis was not included and remains a subject for future work, building upon the partial dynamic modeling presented previously [38].

Future work will focus on extending the finger-level dynamic model and force controller to the entire haptic glove, implementing a multi-finger directional force controller to fully utilize the glove's haptic capabilities, and experimental validation on soft, tumor-like materials. The ultimate goal is to seamlessly integrate the SMU Haptic Glove with 3D elastographic models that will enable accurate and realistic virtual palpation of medical scans.

Preprint not peer reviewed

This preprint research paper has not been peer reviewed. Electronic copy available at: https://ssrn.com/abstract=6350469

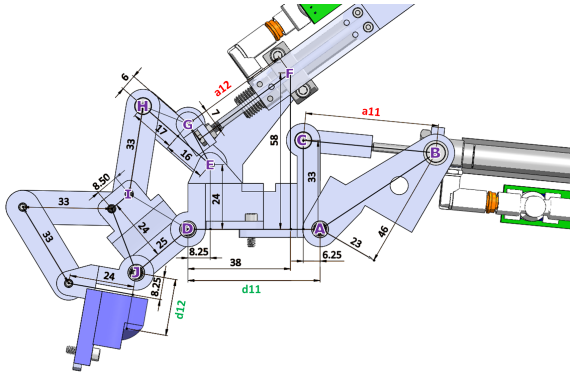

Figure 17: Index substructure geometry detail.

A. Kinematic Analysis

The detailed geometry of the index finger substructure, used for the kinematic analysis, is shown in Fig. 17. The analysis uses two effective length parameters, a_{11} and a_{12} defined as follows:

- The parameter a_{11} represents the total variable distance between points B and C. This length is a direct function of the proximal actuator's displacement and serves as an effective link in the kinematic chain.
- Similarly, a_{12} represents the effective distance from point F to the distal coupler. This length is determined by the displacement of the distal actuator plus a fixed 7 mm mechanical offset relative to point G.

Defining θ_{11} as the flexion of the metacarpophalangeal joint from an open palm, we have

$$\begin{aligned} \theta_{11} &= \tan^{-1}\left(\frac{46}{23}\right) + \angle BAC + \tan^{-1}\left(\frac{33}{6.25}\right) - \pi, \\ \theta_{11} &= \cos^{-1}\left(1.092 - 2.895\times10^{-4} a_{11}^2\right) - 0.207\,\pi. \end{aligned} \tag{8}$$

where the $\angle BAC$ can be found using the law of cosines as follows:

$$\angle BAC = \cos^{-1}\left(\frac{(23^2+46^2)+(6.25^2+33^2)-a_{11}^2}{2\sqrt{23^2+46^2}\sqrt{6.25^2+33^2}}\right) \tag{9}$$

The phalanx shells and their supporting arms are designed with bilateral symmetry, ensuring that connection angles $\angle DEH$, $\angle DIH$ are always equal. This property holds for all such linkages in the design. For the kinematic model, we define the angle at the gearing interface, $\angle DEH$ as θ_{1g}. This parameter is then used to calculate the distal interphalangeal joint angle θ_{12}.

$$\begin{aligned} \theta_{1g} &= \angle DEH = 2\,\pi - \angle DEF - \angle FEG - \tan^{-1}(\frac{6}{16}), \\ \theta_{1g} &= \sin^{-1}\left(1.479 - 6.477\times10^{-4} a_{12}^2\right) + 0.509\,\pi. \end{aligned} \tag{10}$$

Where $\angle FEG$ and $\angle DEF$ can be defined using a very similar approach as before,

$$\angle FEG = \cos^{-1}\left(\frac{((38-8.25)^2+(58-24)^2+(6^2+16^2)-(a_{12}^2+7^2))}{2\sqrt{(38-8.25)^2+(58-24)^2}\sqrt{6^2+16^2}}\right) \tag{11}$$

$$\angle DEF = \cos^{-1}\left(\frac{(8.25^2+24^2)+((38-8.25)^2+(58-24)^2)-(38^2-58^2)}{2\sqrt{8.25^2+24^2}\sqrt{(38-8.25)^2+(58-24)^2}}\right) \tag{12}$$

Defining θ_{12} as the flexion of one of the interphalangeal joints (which are forced to be equal by the gearing mechanism) from an open palm, we have

$$\begin{aligned} \theta_{12} &= 2\tan^{-1}\left(\frac{24}{8.5}\right) + \angle EDI - \pi, \\ \theta_{12} &= 2\cos^{-1}\left(\frac{25.38 - 33\cos\theta_{1g}}{\sqrt{1733.06 - 1674.97\cos\theta_{1g}}}\right) - 0.210\,\pi. \end{aligned} \tag{13}$$

Where $\angle EDI$ can be computed by symmetry $\angle EDI = 2\angle EDH$, as

$$\angle EDI = 2\cos^{-1}\left(\frac{\overline{DH} + (8.25^2+24^2) - 33^2}{2\overline{DH}\sqrt{8.25^2+24^2}}\right) \tag{14}$$

$$\overline{DH} = \sqrt{33^2 + (8.25^2+24^2) - 2(33)\sqrt{8.2562+24^2}cos\theta_{1g}} \tag{15}$$

References

[1] Baik, S., Park, S., Park, J., 2020. Haptic glove using tendon-driven soft robotic mechanism. Frontiers in bioengineering and biotechnology 8, 541105.

[2] Bartalucci, L., Secciani, N., Brogi, C., Topini, A., Della Valle, A., Ridolfi, A., Allotta, B., 2023. An original mechatronic design of a kinaesthetic hand exoskeleton for virtual reality-based applications. Mechatronics 90, 102947.

[3] Ben-Tzvi, P., Ma, Z., 2014. Sensing and force-feedback exoskeleton (safe) robotic glove. IEEE Transactions on Neural Systems and Rehabilitation Engineering 23, 992–1002.

[4] Bickley, L., Szilagyi, P.G., 2012. Bates' guide to physical examination and history-taking. Lippincott Williams & Wilkins.

[5] Blake, J., Gurocak, H.B., 2009. Haptic glove with MR brakes for virtual reality. IEEE/ASME Transactions On Mechatronics 14, 606–615.

[6] Bouzit, M., Burdea, G., Popescu, G., Boian, R., 2002. The Rutgers Master II-new design force-feedback glove. IEEE/ASME Transactions on mechatronics 7, 256–263.

[7] Choi, I., Hawkes, E.W., Christensen, D.L., Ploch, C.J., Follmer, S., 2016. Wolverine: A wearable haptic interface for grasping in virtual reality, in: 2016 IEEE/RSJ International Conference on Intelligent Robots and Systems (IROS), IEEE. pp. 986–993.

[8] Correas, J.M., Tissier, A.M., Khairoune, A., Khoury, G., Eiss, D., Hélénon, O., 2013. Ultrasound elastography of the prostate: state of the art. Diagnostic and interventional imaging 94, 551–560.

[9] CyberGlove Systems LLC, 2017. CyberGlove Systems LLC. URL: https://www.cyberglovesystems.com/.

[10] Demain, S., Metcalf, C.D., Merrett, G.V., Zheng, D., Cunningham, S., 2013. A narrative review on haptic devices: relating the physiology and psychophysical properties of the hand to devices for rehabilitation in central nervous system disorders. Disability and Rehabilitation: Assistive Technology 8, 181–189.

[11] Dexta Robotics, 2025. Dexmo - Dexta Robotics.

[12] Enayati, N., De Momi, E., Ferrigno, G., 2016. Haptics in robot-assisted surgery: Challenges and benefits. IEEE reviews in biomedical engineering 9, 49–65.

[13] Endo, T., Kawasaki, H., Mouri, T., Ishigure, Y., Shimomura, H., Matsumura, M., Koketsu, K., 2010. Five-fingered haptic interface robot: HIRO III. Issue: 1 Publisher: IEEE.

Preprint not peer reviewed

This preprint research paper has not been peer reviewed. Electronic copy available at: https://ssrn.com/abstract=6350469

[14] Fontana, M., Fabio, S., Marcheschi, S., Bergamasco, M., 2013. Haptic hand exoskeleton for precision grasp simulation. Journal of Mechanisms and Robotics 5, 041014.
[15] Galla, M.E., Al Khatib, E.I., Richer, E., Hurmuzlu, Y., 2020. Design and nonlinear control of a haptic glove for virtual palpation, in: 2020 American Control Conference (ACC), IEEE. pp. 551–556.
[16] Gani, A., Pickering, O., Ellis, C., Sabri, O., Pucher, P., 2022. Impact of haptic feedback on surgical training outcomes: a randomised controlled trial of haptic versus non-haptic immersive virtual reality training. Annals of Medicine and Surgery 83, 104734.
[17] Gennisson, J.L., Deffieux, T., Fink, M., Tanter, M., 2013. Ultrasound elastography: principles and techniques. Diagnostic and interventional imaging 94, 487–495.
[18] Greiner, T.M., 1991. Hand anthropometry of US army personnel. US Army Natick Research, Development & Engineering Center.
[19] Gu, X., Zhang, Y., Sun, W., Bian, Y., Zhou, D., Kristensson, P.O., 2016. Dexmo: An inexpensive and lightweight mechanical exoskeleton for motion capture and force feedback in VR, in: Proceedings of the 2016 CHI Conference on Human Factors in Computing Systems, pp. 1991–1995.
[20] Hardin Jr, D.M., 1999. Acute appendicitis: review and update. American family physician 60, 2027–2034.
[21] Iqbal, J., Tsagarakis, N., Caldwell, D., 2014. Human hand compatible underactuated exoskeleton robotic system. Electronics Letters 50, 494–496. doi:10.1049/el.2014.0508.
[22] Iqbal, J., Tsagarakis, N., Caldwell, D., 2015. Four-fingered lightweight exoskeleton robotic device accommodating different hand sizes. Electronics Letters 51, 888–890.
[23] Jones, L.A., Lederman, S.J., 2006. Human hand function. Oxford university press.
[24] Kennedy, P., Wagner, M., Castéra, L., Hong, C.W., Johnson, C.L., Sirlin, C.B., Taouli, B., 2018. Quantitative elastography methods in liver disease: current evidence and future directions. Radiology 286, 738–763.
[25] Koyama, T., Yamano, I., Takemura, K., Maeno, T., 2002. Multi-fingered exoskeleton haptic device using passive force feedback for dexterous teleoperation, in: IEEE/RSJ International Conference on Intelligent Robots and Systems, IEEE. pp. 2905–2910.
[26] Le, D.T.G., Nguyen, L., 2021. An efficient force-feedback hand exoskeleton for haptic applications. International Journal of Intelligent Robotics and Applications 5, 395–409.
[27] Li, H., Cheng, L., 2024. A Systematic Review on Hand Exoskeletons From the Mechatronics Aspect. IEEE/ASME Transactions on Mechatronics .
[28] Ma, Z., Ben-Tzvi, P., 2015. Design and optimization of a five-finger haptic glove mechanism. Journal of Mechanisms and Robotics 7, 041008.
[29] McKnight, A.L., Kugel, J.L., Rossman, P.J., Manduca, A., Hartmann, L.C., Ehman, R.L., 2002. MR elastography of breast cancer: preliminary results. American journal of roentgenology 178, 1411–1417.
[30] Michikawa, R., Endo, T., Matsuno, F., 2022. A Multi-DoF Exoskeleton Haptic Device for the Grasping of a Compliant Object Adapting to a User's Motion Using Jamming Transitions. IEEE Transactions on Robotics 39, 373–385.
[31] Palmerius, K.L., Havre, R.F., Gilja, O.H., Viola, I., 2011. Ultrasound palpation by haptic elastography, in: 2011 24th International Symposium on Computer-Based Medical Systems (CBMS), IEEE. pp. 1–6.
[32] Park, Y., Jo, I., Bae, J., 2016. Development of a dual-cable hand exoskeleton system for virtual reality, in: 2016 IEEE/RSJ International Conference on Intelligent Robots and Systems (IROS), IEEE. pp. 1019–1024.
[33] Park, Y., Jo, I., Lee, J., Bae, J., 2020. WeHAPTIC: a wearable haptic interface for accurate position tracking and interactive force control. Mechanism and Machine Theory 153, 104005.
[34] Peng, S., Yu, M., Geng, X., Cheng, X., Wang, P., 2023. A lightweight exoskeleton force feedback glove, in: Actuators, MDPI. p. 199.
[35] Pepin, K.M., Ehman, R.L., McGee, K.P., 2015. Magnetic resonance elastography (MRE) in cancer: Technique, analysis, and applications. Progress in nuclear magnetic resonance spectroscopy 90, 32–48.
[36] Perret, J., Vander Poorten, E., 2018. Touching virtual reality: a review of haptic gloves, in: ACTUATOR 2018; 16th International Conference on New Actuators, VDE. pp. 1–5.
[37] Rago, T., Santini, F., Scutari, M., Pinchera, A., Vitti, P., 2007. Elastography: new developments in ultrasound for predicting malignancy in thyroid nodules. The Journal of Clinical Endocrinology & Metabolism 92, 2917–2922.
[38] Richer, E., Galla, M., Hurmuzlu, Y., 2023. Directional Force Feedback for a 3 DOF Pneumatic Haptic Finger. IFAC-PapersOnLine 56, 295–300.
[39] Sarakoglou, I., Brygo, A., Mazzanti, D., Hernandez, N.G., Caldwell, D.G., Tsagarakis, N.G., 2016. Hexotrac: A highly under-actuated hand exoskeleton for finger tracking and force feedback, in: 2016 IEEE/RSJ International Conference on Intelligent Robots and Systems (IROS), IEEE. pp. 1033–1040.
[40] Suarez-Escobar, M., Gallego-Sanchez, J.A., Rendon-Velez, E., 2017. Mechanisms for linkage-driven underactuated hand exoskeletons: conceptual design including anatomical and mechanical specifications. International Journal on Interactive Design and Manufacturing (IJIDeM) 11, 55–75.
[41] Ullrich, S., Kuhlen, T., 2012. Haptic palpation for medical simulation in virtual environments. IEEE Transactions on Visualization and Computer graphics 18, 617–625.
[42] Wang, D., Song, M., Naqash, A., Zheng, Y., Xu, W., Zhang, Y., 2018. Toward whole-hand kinesthetic feedback: A survey of force feedback gloves. IEEE transactions on haptics 12, 189–204.
[43] Wang, Z., Wang, D., Zhang, Y., Liu, J., Wen, L., Xu, W., Zhang, Y., 2019. A three-fingered force feedback glove using fiber-reinforced soft bending actuators. IEEE Transactions on Industrial Electronics 67, 7681–7690.
[44] Williams, R.L., Srivastava, M., Howell, J.N., Conatser Jr, R.R., Eland, D.C., Burns, J.M., Chila, A.G., 2004. The virtual haptic back for palpatory training, in: Proceedings of the 6th international conference on Multimodal interfaces, pp. 191–197.
[45] Yacoub, A., Richer, E., Hurmuzlu, Y., 2025. Comparative Analysis of Fingertip Location for the SMU Haptic Glove by OptiTrack Cameras and Embedded Position Sensors. IFAC-PapersOnLine 59, 203–208.
[46] Zhang, R., Kunz, A., Lochmatter, P., Kovacs, G., 2006. Dielectric elastomer spring roll actuators for a portable force feedback device, in: 2006 14th Symposium on Haptic Interfaces for Virtual Environment and Teleoperator Systems, IEEE. pp. 347–353.
[47] Zheng, Y., Wang, D., Wang, Z., Zhang, Y., Zhang, Y., Xu, W., 2018. Design of a lightweight force-feedback glove with a large workspace. Engineering 4, 869–880.
[48] Zhou, M.A., Ben-Tzvi, P., 2014. RML glove—An exoskeleton glove mechanism with haptics feedback. Issue: 2 Publisher: IEEE.
[49] Zubrycki, I., Granosik, G., 2015. Novel haptic glove-based interface using jamming principle, in: 2015 10th International Workshop on Robot Motion and Control (RoMoCo), IEEE. pp. 46–51.

Ammar Yacoub received a B.S. degree in Mechatronics Engineering from the University of Jordan and an M.S. in Mechanical/Mechatronics Engineering from Jordan University of Science and Technology. He is currently pursuing a Ph.D. in Mechanical Engineering at the Systems Laboratory, Southern Methodist University in Dallas, TX, USA. His primary research is in robotics and control, focusing on haptic-assisted robotic systems.

Edmond Richer received the M.S. degree in mechanical engineering from the University of Craiova, Craiova, Romania, in 1988, and the Ph.D. degree in dynamic systems and control from the Lyle School of Engineering, Southern Methodist University, Dallas, TX, USA, in 1998. He currently directs the Biomedical Instrumentation and Robotics Laboratory and is an Associate Professor with the Lyle School of Engineering, Southern Methodist University. His current research interests include advanced dynamics and control, image-guided and haptic-assisted robotic systems, and ultrasound applications in bone quality assessment and super-resolution imaging.

This preprint research paper has not been peer reviewed. Electronic copy available at: https://ssrn.com/abstract=6350469

Yildirim Hurmuzlu received his B.S. degree from Bogazici University in 1981, and his M.S. and Ph.D. degrees from Drexel University in 1983 and 1987 all in Mechanical Engineering. Since 1987, he has been at Southern Methodist University, Dallas, Texas, where he is a University Distinguished Professor in the Department of Mechanical Engineering and also served as department chair for seven years. His research focuses on nonlinear dynamical systems and control, with emphasis on robotics, biomechanics, and vibration control. Dr. Hurmuzlu is an ASME fellow and an IEEE senior member. He has been in the past associate Editor of the ASME Transactions on Dynamics Systems, Measurement and Control and IEEE/ASME Transaction on Mechatronics. He is presently on the editorial board of Actuators and Machines Journals.

Preprint not peer reviewed

This preprint research paper has not been peer reviewed. Electronic copy available at: https://ssrn.com/abstract=6350469